Proceedings of HT-FED 2004
2004 ASME Heat Transfer/Fluids Engineering Summer Conference
Charlotte, North Carolina, USA, July 11-15, 2004

HT-FED2004-56350

NON-BOUNDARY CONFORMING METHODS FOR LARGE-EDDY SIMULATIONS OF BIOLOGICAL FLOWS

Elias Balaras*
Department of Mechanical Engineering
University of Maryland
College Park, MD 20742
Email: balaras@eng.umd.edu

Jianming Yang
Department of Mechanical Engineering
University of Maryland
College Park, MD 20742
Email: jmyang@glue.umd.edu

ABSTRACT

In the present paper a computational algorithm suitable for large-eddy simulations of fluid/structure problems that are commonly encountered in biological flows is presented. It is based on a mixed Eurelian-Lagrangian formulation, where the governing equations are solved on a fixed grid, which is not aligned with the body surface, and the non-slip conditions are enforced via local reconstructions of the solution near the solid interface. With this strategy we can compute the flow around complex stationary/moving boundaries and at the same time maintain the efficiency and optimal conservation properties of the underlying Cartesian solver. A variety of examples, that establish the accuracy and range of applicability of the method are included.

INTRODUCTION

Today, due to the impressive advancements in high performace parallel computing the large-eddy simulation (LES) approach has emerged as valuable tool for turbulence research and has contributed invaluable information on the structure and dynamics of a variety of flows which are of engineering interest. There are, however, applications from biology and physiology where the use of LES has received considerably less attention as a result of exceedingly complex fluid/structure interactions that dominate the dynamics of these flows. Characteristic examples include the flow of blood in the heart or around medical implants, insect locomotion and bird flight. Massive computations using LES can contribute to a new fundamental understanding of the dynamics of such flows and help bring to fruition novel devices.

From scaling considerations of the required spatial and temporal resolution, LES of such flows are well within reach of today's supercomputers. On the other hand, these class of problems introduce new challenges to high-fidelity numerical methods since the flow is highly unsteady and involves moving and/or deforming boundaries composed of anisotropic non-linear materials. Boundary conforming methods that are traditionally employed in complex geometrical configurations have been successfully extended to problems involving moving boundaries. While such methods have been demonstrated to be very effective in creeping and low Reynolds number problems (see for example [1, 2]), little work has been completed for moderate/high Reynolds number flows because of the associated computational cost and resolution constraints [3, 4]. Considering work that has been completed for turbulent flows, most of the developments have been done in the framework of the Reynolds Averaged Navier Stokes (RANS) approach (i.e. [5,6]). These schemes typically employ stable, dissipative discretizations, making their use in LES problematic.

An attractive alternative, which can be a cost/effective strategy in a variety of biological flows, are non-boundary conforming methods. In such case the equations governing the fluid flow are solved on a fixed Cartesian grid. The effect of a stationary or moving boundary, which in this case does not coincide with the grid, is introduced through proper treatment of the solution variables at the cells in the vicinity of the boundary. An advantage of this type of methods is that the need for grid regeneration

*Address all correspondence to this author.

or deformation is eliminated, and highly efficient solvers can be used with minimal changes. In terms of the imposition of boundary conditions there are two broad categories of methods that are usually adopted: *Cartesian* or *cut-cell* methods and *immersed boundary* methods.

In *Cartesian* methods a solid boundary is tracked as a sharp interface and the grid cells at the body interface are modified according to their intersections with the underlying Cartesian grid. Using proper interpolation strategies the flow variables on the modified cells can be computed according to the boundary conditions on the body. *Cartesian* methods allow for a clear distinction between the solid and the fluid by practically generating a boundary-fitted grid around the body. Successful applications of such methods for a variety of flow problems can be found in [7, 8]. However, due the variaty of possible intersections between the grid and the boundary a large number of 'interface-cells' is generated leading to an equally large number of 'special treatments'. Also in complex configurations the unavoidable generation of irregularly shaped cells with very small size can have an adverse impact of the conservation and stability properties of the solver. Recently Ye *et al.* [9] suggested a cell merging scheme to address this problem. This formulation was also extended to treat moving boundaries with good results for a variety of two-dimensional problems [10]. The extention of the methodology in complex three-dimensional configurations remains to be investigated.

In *immersed boundary* formulations the governing equations are discretized on a fixed Cartesian grid, but in this case the effect of a stationary or moving boundary is introduced through an external force field. The method has been introduced by Peskin [11] in the beginning of the 70^s to study blood flow in the heart [12, 13]. In these computations the motion of the boundary was determined by the fluid itself, and vice-verca. The vascular boundary was modeled as a set of elements linked by springs, and a Lagrangian coordinate system was attached to track their location in space. The tracking information was then used to compute the proper structure of the external force field that was introduced to the underline Eulerian grid on which the governing equation for the fluid flow are solved. A disadvantage of the above formulation is the need to distribute the forcing over $3-4$ grid nodes (usually through a discrete delta function), which unavoidably introduces some blurring between the fluid and the solid. This feature increases substantially the resolution requirements, and appears to be a major obstacle in the extention of the method to LES, where the proper representation of the thin shear layers near a solid body is crucial for the accuracy of the computations.

To overcame this limitation Mohd-Yusof [14] and Fadlun *et al.* [15] proposed a methodology where the forcing function is considered in the framework of the discretized equations of motion. This formulation introduces a set of discrete body-forces at the grid nodes nearest to the boundary, which is practically equivalent to a local reconstruction of the solution based on the target boundary values. To this respect the method can be viewed as a hybrid Cartesian/Immersed boundary formulation since it shares features with both approaches. The method has been successfully applied to a variety of problems including large-eddy simulation (LES) of turbulent flow inside a motored IC piston/cylinder assembly [15].

Central to the accuracy of the above formulation is the way the solution is reconstructed near the boundary. Fadlun *et al.* [15] suggested a simple one-dimensional scheme, where the solution is reconstructed along an arbitrary grid line. The method is straightforward, second order accurate and works well for bodies that are largely aligned with the grid lines. In cases of complex bodies the choice of the reconstruction direction at several points in the flow field can be arbitrary. Multidimensional schemes can remove this limitation. Kim *et al.* [16] suggested a hybrid scheme, which uses a bilinear reconstruction procedure that is however, reduced to a one-dimensional linear one, when there are no available points in the vicinity of the boundary to support the 2D stencil. Balaras [17] introduced a more general scheme which is applicable to complex boundaries without special treatments, since the reconstruction is always performed at the well defined line normal to the interface. The scheme was tested in a variety of laminar and turbulent flows with very good results. In the present paper an extention of the work in [17] to moving boundaries is presented. Examples of laminar and turbulent flows are included to establish the accuracy and range of applicability of the method.

NUMERICAL METHOD
Basic Solver

In LES, the resolved, large-scale, velocity and pressure fields can be obtained from direct solution of the filtered Navier-Stokes equations, where scales smaller than the grid size are modeled. In the present, finite-difference implementation, a top-hat filter in physical space that is implicitly applied by the finite-difference operators separates the resolved from unresolved scales. The resulting subgrid scale (SGS) stresses are modeled using the lagrangian dynamic eddy-viscosity model [18]. Details on the present implementation of the model together with an evaluation of its accuracy in equilibrium and non-equilibrium flows, is given in [19].

The equations governing the evolution of the large scales are solved on an underlying grid (in Cartesian or cylindrical coordinates) that covers the entire computational domain without the bodies. Integration is done using a fractional-step method, with an implicit Crank-Nicolson scheme for the viscous terms and a third-order Runge-Kutta (RK3) explicit scheme for all other terms. All spatial derivatives are approximated with second order central differences on a staggered grid. The large-band matrix associated to the solution of the Poisson equation is inverted using direct methods. The above procedure can be summarized into the following steps:

$$\frac{\hat{u}_i^k - u_i^{k-1}}{\Delta t} = -\left[\gamma_k A\left(u_i^{k-1}\right) + \rho_k A\left(u_i^{k-2}\right)\right] + \frac{1}{2}\alpha_k\left[B\left(\hat{u}_i^k\right) + B\left(u_i^{k-1}\right)\right] - \alpha_k \frac{\partial p^{k-1}}{\partial x_i} + f_i^k, \qquad (1)$$

$$\nabla^2 \phi^k = \frac{1}{\alpha_k \Delta t}\frac{\partial \hat{u}_i^k}{\partial x_i}, \qquad (2)$$

$$u_i^k = \hat{u}_i^k - \alpha_k \Delta t \frac{\partial \phi^k}{\partial x_i}, \qquad (3)$$

$$p^k = p^{k-1} + \phi^k - \frac{\alpha_k \Delta t}{2Re}\frac{\partial^2 \phi^k}{\partial x_i^2}, \qquad (4)$$

where $\hat{u}_i^k$ is the intermediate velocity and ϕ is the pressure correction. Operator A represents the terms treated explicitly, and B the ones treated implicitly. f_i^k is the momentum forcing adopted to enforce proper boundary conditions on immersed boundaries and will be discussed in the next section. Δt is the time step and k is the sub-step index ($k = 1,3$). The RK3 coefficients are $\alpha_1 = 8/15$, $\gamma_1 = 8/15$, $\rho_1 = 0$; $\alpha_2 = 2/15$; $\gamma_2 = 5/12$, $\rho_2 = -17/60$;$\alpha_3 = 1/3$, $\gamma_3 = 3/4$, $\rho_3 = -5/12$.

Treatment of Immersed Boundaries

To compute the flow around complex objects which are not aligned with the grid, we have developed a methodology that practically reconstructs the solution in the vicinity of the body according to the target boundary values [17]. The approach, which is based on the ideas in [14, 15], allows for a precise imposition of the boundary conditions without compromising the accuracy and efficiency of the solver. In particular, the application of velocity boundary conditions on a body immersed in the Cartesian grid involves the following steps: (a) Identification of the interface between the body and the fluid; (b) Establishment of the grid/interface relation and identification of the points in the solution variable grid where boundary conditions will be enforced; (c) Reconstruction of the solution on the above points. For steps (a) and (b), which are usually referred to as ‘interface tracking’, a scheme based on algorithms devised for solidification problems and multiphase flow dynamics [20, 21] is used. With this approach, an immersed boundary of arbitrary shape is identified by a series of material-fixed interfacial markers whose location

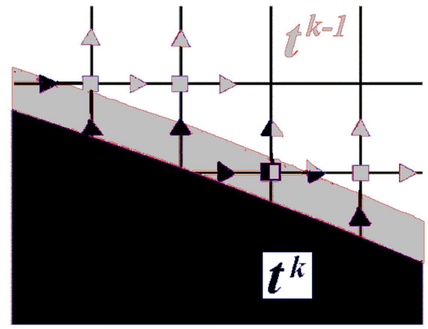

Figure 1. STAGGERED GRID ARRANGEMENT NEAR THE BODY FOR THE 2D PROBLEM. GREY AREA DENOTES THE LOCATION OF THE BODY AT t^{k-1} AND BLACK AT t^k; $\square$ p; $\triangle$ u_i.

is defined in the reference configuration of the solid. This information is then used to identify the Eulerian grid nodes involved in the reconstruction of the solution near the boundary in a way that the desired boundary conditions for the fluid are satisfied to the desired order of accuracy. The reconstruction is performed ‘around’ the points in the fluid phase closest to the solid boundary (all points that have least one neighbor in the solid phase). In the framework of the present fractional step method the imposition of boundary conditions on an immersed boundary is equivalent to the addition to equation (1) of a forcing term of the form:

$$f_i^k = \frac{\hat{V}_i^k - u_i^{k-1}}{\Delta t} + \left[\gamma_k A\left(u_i^{k-1}\right) + \rho_k A\left(u_i^{k-2}\right)\right] - \frac{1}{2}\alpha_k\left[B\left(\hat{u}_i^k\right) + B\left(u_i^{k-1}\right)\right] + \alpha_k \frac{\partial p^{k-1}}{\partial x_i} \qquad (5)$$

where $\hat{V}_i^k$ is the reconstructed intermediate velocity, such that the desired boundary conditions are satisfied on the immersed boundary. The details on the tracking scheme and the solution reconstruction for stationary boundaries can be found in [17].

When the immersed boundary moves, the role of several computational nodes in the vicinity of the boundary changes. This is illustrated in Figure 1, where the the boundary moves from its position at time step t^{k-1} (grey shadow region) to a new position at time step t^k (black shadow region). Some velocity nodes (hereinafter referred as ‘boundary’ points), which were central to the reconstruction of the solution, become interior ‘fluid’ points. In addition, other nodes inside the body (hereinafter referred as ‘body’ points) at time step t^{k-1} emerge into the fluid and become ‘boundary’ points at t^k. The latter family of points does not require any special treatment because the solution at t^k would be reconstructed based on known values. On the other hand, the former family of points introduces prob-

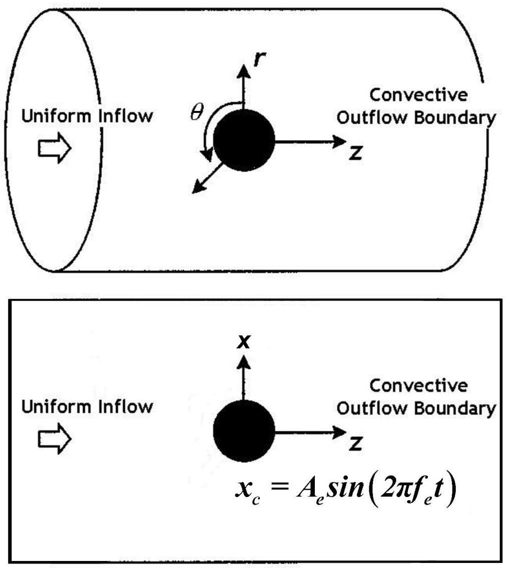

Figure 2. SKETCH OF COMPUTATIONAL DOMAIN FOR THE CASE OF THE SPHERE (TOP) AND OSCILLATING CYLINDER (BOTTOM).

lems when computing the *RHS* of equation (1) at t^k: all the grid nodes that were 'boundary' points at t^{k-1} would have the correct value of u_i^{k-1} (this is the boundary condition that was enforced at t^{k-1}), but most derivatives of u_i^{k-1} would be incorrect since they involve points previously in the interior of the body. To alleviate this problem the velocity and pressure at these points is 'extended' to the interior of the body at time t^{k-1}, using 2^{nd} order multidimensional reconstructions [22].

RESULTS

Numerical Examples of Laminar Flows

To verify the accuracy of the proposed methodology, initially a series of computations of laminar flows, for which detailed numerical and experimental data are available in the literature, is conducted. Two cases are presented in this section that involve both stationary and moving immersed boundaries: the three-dimensional flow around a sphere, and two-dimensional flow around a cylinder oscillating in a cross flow.

A schematic of the computational domain for the flow around the sphere is shown in Figure 2. Cylindrical coordinates are used for a more efficient distribution of the grid points. Computations have been conducted for Reynolds numbers ($Re = UD/\nu$, where U is the freestream velocity, D the diameter of the sphere) ranging from 50 to 300. The flow is steady and axisymmetric for Reynolds numbers up to 200, while for the highest Reynolds number ($Re = 300$) the flow is unsteady and is dominated by vortex shedding. The size of the computational box in the streamwise direction is $30D$ with the sphere located in the middle, and $15D$ in the radial direction. To investigate the influence of grid resolution on the results three different grids have been considered for the low Reynolds number cases ($Re = 50$ to 200). Grid 1 involves $100 \times 40 \times 40$ computational points in the streamwise, radial and azimuthal directions respectively. In the other two cases the grid is refined in the streamwise and radial directions (Grid 2: $200 \times 40 \times 80$ and Grid 3: $400 \times 40 \times 160$ respectively). All three grids are stretched in the streamwise and radial directions to cluster points near the surface of the sphere. The resulting average grid spacing near the sphere for the three different resolutions is approximately $0.1D$, $0.05D$ and $0.025D$ respectively. The computations for $Re = 300$ case are performed on single refined grid involving $420 \times 64 \times 112$ nodes. With this resolution approximately 10 grid points are located in the boundary layers near the stagnation point. In all cases a uniform velocity field is specified at the inflow plane. A convective boundary condition is used at the outflow boundary [23], and radiative boundary conditions are applied at the freestream boundary.

Table 1 shows the present results in comparison with the experimental results in [24], and the well resolved simulations by Johnson and Patel [25] where body-fitted grids are used. For all Reynolds numbers and grid resolutions the main features of the flow are properly captured. The drag coefficient on the coarsest grid, is a little higher (approximately 8%) in comparison with the reference experimental and numerical data. As the grid is refined, however, the agreement is very good. The error in drag coefficient, which is computed using the experimental results in [24] as the reference values, as a function of grid spacing near the sphere is shown in Figure 3. It can be seen that the error reduces with a second order slope, which is consistent with the order of accuracy of the method.

A more challenging test for the present methodology is the case at $Re = 300$, where the flow becomes unsteady and the wake is dominated by periodic vortex shedding. The vortical structures in the wake are shown in Figure 4, where iso-surfaces of the second invariant of the velocity gradient tensor (or 'Q' criterion [26]) are used for their visualization. Hairpin like vortices originating from the surface of the sphere can be observed, with

Table 1. PREDICTION OF C_D FOR THE CASE OF THE SPHERE

Re	50	100	150	200
Grid 1	1.707	1.229	1.045	0.945
Grid 2	1.609	1.118	0.919	0.807
Grid 3	1.586	1.095	0.894	0.776
Experiment [24]	1.574	1.087	0.889	0.776
Ref. simulation [25]	1.575	1.100	0.900	0.775

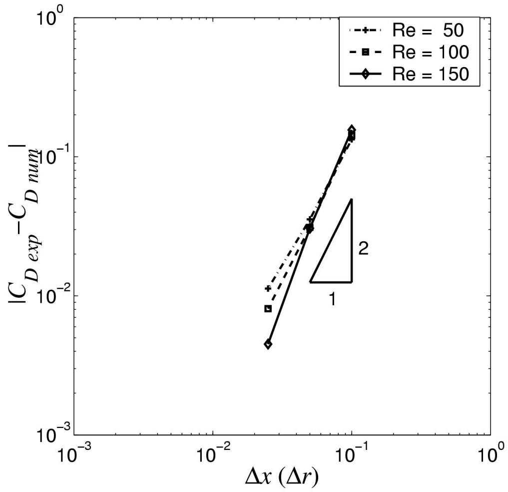

Figure 3. ERROR IN THE DRAG COEFFICIENT FOR THE FLOW AROUND THE SPHERE AS A FUNCTION OF GRID RESOLUTION.

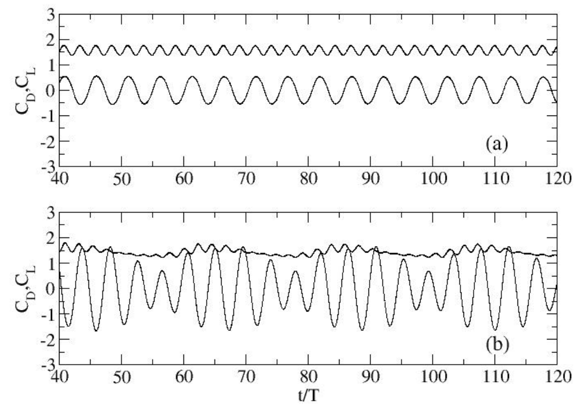

Figure 5. TEMPORAL EVOLUTION OF THE LIFT AND DRAG COEFFICIENTS FOR THE CASE OF THE CYLINDER OSCILLATING IN A CROSS FLOW. (a) $f_e/f_o = 1.0$; (b) $f_e/f_o = 1.2$. ——— C_D; - - - C_L

new vortical structures developing around their legs as they are convected downstream. This behavior is nearly the same as the one shown in [25] indicating that the present method properly captures the three-dimensional vorticity field. The values of the drag and lift coefficient are also in excellent agreement with the reference data. In particular, the predicted drag and lift coefficients are $C_D = 0.655$ and $C_L = 0.064$ respectively, which are within 1% to the values reported in [24] and [25]).

To evaluate the accuracy of the method for the case of moving boundaries the flow around a cylinder oscillating transversally in a free-stream is computed. All flow parameters are chosen to replicate the conditions in the simulations reported in [27], where very fine body-fitted grids are used. The Reynolds number ($Re = UD/\nu$, where U is the freestream velocity and D the cylinder diameter) is 185. Other important parameters are the oscillation frequency f_e and amplitude A_e. In all computations the motion of the cylinder is given by a simple harmonic function $x_c = A_e sin(2\pi f_e t)$, with $A_e = 0.2$. A variety of frequencies is considered ranging from $f_e/f_o = 0.8$ to $f_e/f_o = 1.2$, where f_o is the natural shedding frequency of the stationary cylinder at the same Reynolds number. The size of the computational box is $50D \times 30D$ in the streamwise and crossstream directions respectively, with the cylinder located $20D$ from the inflow plane (Figure 2). As for the case of the sphere a uniform velocity field is specified at the inflow plane, and convective and radiative boundary conditions are used at the outflow and freestream boundaries respectively. All computations are performed on a non-uniform grid involving 300×300 points. The average grid spacing near the cylinder surface is of the order of $0.01D$.

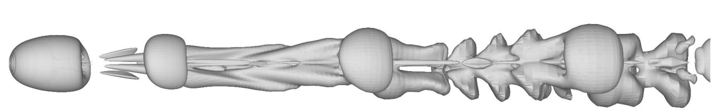

Figure 4. VORTICAL STRUCTURES IN THE WAKE OF THE SPHERE FOR $Re = 300$. ISO-SURFACES OF $Q = 0.001$ ARE SHOWN.

The temporal variation of the lift and drag coefficients changes substantially when the excitation frequency is varied near the natural shedding frequency f_o. An example is shown in Figure 5 for $f_e/f_o = 1.0$ and $f_e/f_o = 1.2$. In the former case a fairly regular behavior of the lift and drag coefficients can be observed once vortex shedding is established. In the latter the appearance of a higher harmonic is apparent. This behavior has also been observed in previous experimental and numerical studies and can be attributed to the change in sign of the energy transfer between the fluid and the cylinder. In Figure 6 the mean value of the drag coefficient, $\overline{C}_D$, the root mean square of the drag coefficient, $C_D rms$, and the root mean square of the lift coefficient, $C_L rms$, are shown as a function of the excitation frequency f_e/f_o. The mean value of C_D has a peak at $f_e/f_o = 1.0$, as expected, and then decreases are f_e/f_o increases. $C_L rms$, on the other hand, peaks at $f_e/f_o = 1.1$ where the vortex switching occurs. These results are also in very good quantitative agreement with the corresponding values reported in [27]. In Figure 7 instantaneous spanwise vorticity isolines in four different phases

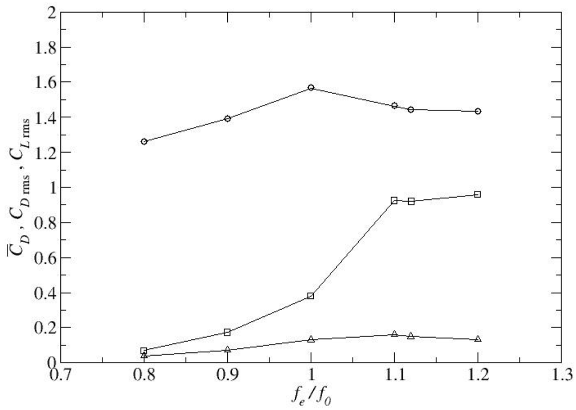

Figure 6. VARIATION OF: ○ $\overline{C}_D$; △ $C_D rms$; □ $C_L rms$ FOR THE CASE OF THE CYLINDER OSCILLATING IN A CROSS FLOW AS A FUNCTION OF f_e/f_o.

during the harmonic oscillation are shown for $f_e/f_o = 1.0$. During the upward motion of the cylinder vorticity is formed at the base, whose sign is opposite to the one in the upper shear layer. Their interaction results in a decrease of the vorticity available for roll-up in the wake.

Pulsatile Flow in a Model of Arterial Stenosis

A more challenging test for the accuracy and efficiency of the present method is the computation of transitional flow in a model of arterial stenosis. Initially a planar model is considered. The constriction is generated by placing two approximately semi-circular sections on the top and bottom walls of a plane channel, resulting in area reduction of 50% (see Figure 8). This choice reduces substantially the cost compared to the axisymmetric case and facilitates a timely examination of all different parameters that affect the dynamics of the flow. Nevertheless, the fundamental dynamics of the flow are similar to the ones observed in axisymmetric experiments reported in the literature.

A schematic of the computational domain is given in Figure 8. The throat of the stenosis and the outflow plane are located $10H$ and $30H$ from inflow plane respectively (H is the channel hight). The spanwise domain size is $3H$, which was found sufficient for the two-point correlations to go to zero. The average Reynolds number during the pulsatile cycle is $Re_b = 1200$ ($Re_b = U_b H/\nu$, where U_b is the average bulk velocity during the cycle, H is the channel hight, and ν is the kinematic viscosity). During one cycle Re_b varies almost sinusoidally with a minimum value of 270 and a maximum of 1500. The corresponding frequency parameter is $\alpha \sim 8$. ($\alpha = h(\omega/\nu)^{1/2}$, where $h = H/2$, and ω is the fundamental pulsatile frequency). The choice of the geometry and parametric space above, mimics closely the conditions in Particle Image Velocimetry (PIV) experiments that were conducted in parallel to the present computations for the purpose of validation of the present method [28]. To establish the grid independency of the solution, computations with different grid resolution in all three coordinate directions involving from 0.5 to 3.0 million points were conducted. It was found the approximately 1.0 million nodes ($360 \times 32 \times 82$ in the streamwise, spanwise and wall-normal directions respectively) was sufficient for that purpose. Periodic boundary conditions are used in the spanwise, homogeneous direction and a convective boundary condition at the outflow plane. At the inflow plane the PIV, phase-averaged, velocity profiles from the experimental study are specified as boundary conditions. Noise with prescribed statistics and spectra has also been added to mimic the disturbance environment in the experiments. The phase-averaged statistics in all computations are extracted over 10 pulsatile cycles. Prior to sampling, 5 cycles were completed for the flow to became independent of the initial conditions.

To visualize the basic dynamics of the flow in the vicinity of the stenosis, spatially and phase-averaged spanwise vorticity isolines are shown in Figure 9 at three characteristic times during the pulsatile cycle. During the initial stages of the accelerating part of the cycle a jet is formed as the flow goes through the constriction (see Figure 9a). The flow at this stage is fairly symmetric. At a letter stage of the same part of the cycle the jet becomes unstable and the shear layers in the proximal post-stenotic area break down generating large spanwise coherent structures (see Figure 9b). These structures are convected downstream interacting with the boundary layers at the walls triggering transition to turbulence. During the decelerating part of the cycle,

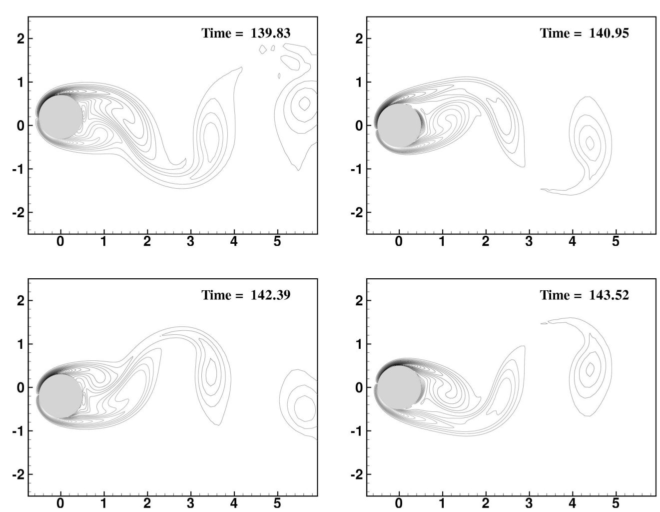

Figure 7. SPANWISE VORTICITY ISOLINES FOR $f_e/f_o = 1.0$

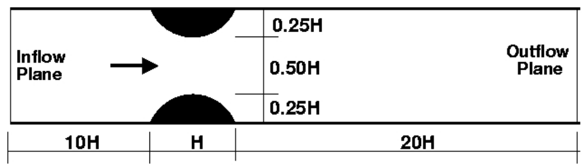

Figure 8. SCHEMATIC OF THE COMPUTATIONAL DOMAIN FOR THE CASE OF FLOW IN A MODEL OF ARTERIAL STENOSIS.

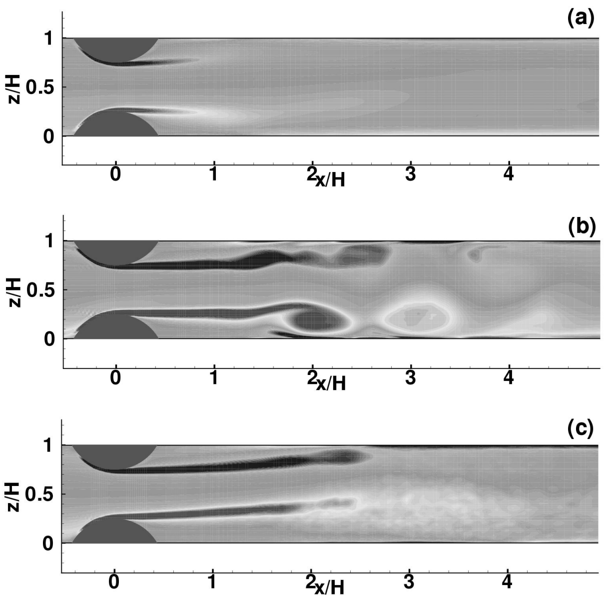

Figure 9. PHASE-AVERAGED SPANWISE VORTICITY DISTRIBUTION. (a) $T = 250^o$; (b) $T = 320^o$; (c) $T = 100^o$. THE ACCELERATING PART OF THE CYCLE IS FROM $T = 180^o$ TO $T = 360^o$ AND THE DECELERATING PART IS FROM $T = 0^o$ TO $T = 180^o$.

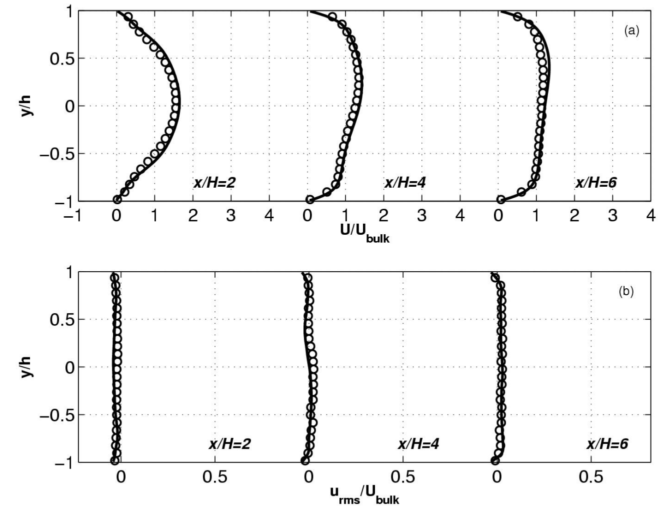

Figure 10. PHASE-AVERAGED STREAMWISE VELOCITY STATISTICS AT $T = 270^o$. ——— simulation; ○ experiment [28]. (a) $< u >$; (b) u_{rms}.

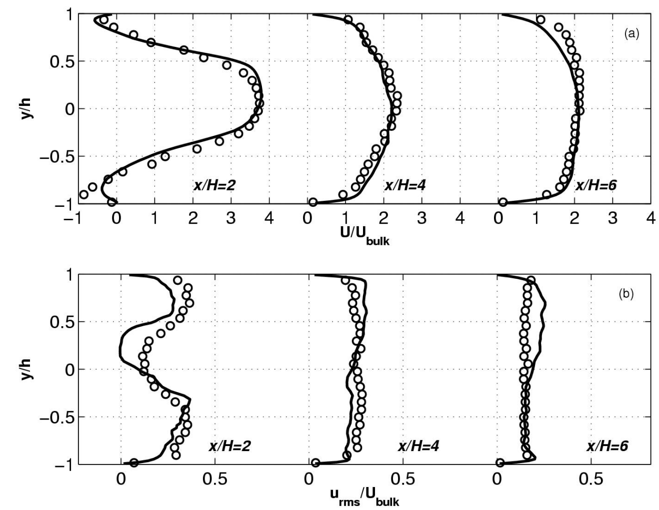

Figure 11. PHASE-AVERAGED STREAMWISE VELOCITY STATISTICS AT $T = 350^o$. ——— simulation; ○ experiment [28]. (a) $< u >$; (b) u_{rms}.

turbulence is enhanced and turbulent boundary layers appear just downstream of the reattachment point. At the same time, very close to the throat of the stenosis the shear layer attaches to one side of the channel (see Figure 9c). This behavior has also been observed in the experiments. In Figures 10 and 11 phase-average profiles of the mean streamwise velocity and velocity fluctuations are shown for $T = 270^o$ and $T = 350^o$ respectively. Both time instances are during the acceleration phase with the latter corresponding to a time just after the breakdown of the shear layer. Three stations in the proximal downstream area are shown: $x/H = 2$, $x/H = 4$ and $x/H = 6$ from the throat of the stenosis. The agreement with the corresponding experimental data is very good.

CONCLUSIONS

In the present paper a methodology to perform LES around complex moving boundaries on fixed grids is presented. The method is based on earlier work reported in [17], and introduces a 'field extention' approach to address problems encountered during the motion of immersed boundaries. Validation is performed for the cases of the flow around a sphere, a cylinder oscillating in a cross-flow and pulsatile flow in a model of arterial stenosis. In all cases the agreement with reference experimental and numerical results is very good.

ACKNOWLEDGMENT

This work is supported by NIH Grant R01-HL-07262. The authors are grateful to Prof. K. Kiger for making the experimental data for the pulsatile stenotic flow available, and to Mr. N. Beratlis for preparing some of the plots in the paper.

REFERENCES

[1] Johnston, A.A. and Tezduyar, D.E. 1997. 3D simulation of fluid-particle interactions with the number of particles reaching 100. *Comput. Methods Appl. Mech. Engrg.*, 145:301–321.

[2] Hu, H. H., Patankar, N. A. and Zhu, M-Y. 2001 Numerical simulations of fluid-solid systems using Arbitrary-Lagrangian-Eulerian technique, *J. Comput. Physics*, 169:427–462.

[3] D.J. Newman and G.E. Karniadakis. 1997. ‘Simulations of flow past a freely vibrating cable. *J. Fluid Mech.*, vol. 344, p. 95, 1997.

[4] C. Evangelinos and G.E. Karniadakis. 1999. Dynamics and flow structures in the turbulent wake of rigid and flexible cylinders subject to vortex-induced vibrations. *J. Fluid Mech.*, vol. 400:91-124.

[5] Ramamurti, R. and Sandberg, W.C. 2001. Computational study of 3D flapping foil flows. *AIAA paper* 2001-0605.

[6] Jouette, C., Laget, O., Gouez, J-M. and Viviand, H. 2002. A dual time stepping method for fluid-structure interaction problems. *Computers & Fluids*, 31:509–537.

[7] De Zeeuw, D., Powell, K.G. 1991. An adaptively refined Cartesian mesh solver for the Euler equations. *AIAA Paper* 91-1542-CP

[8] Quirk, J.J. 1994 An alternative to unstructured grids for computing gas dynamic flows around arbitrary two-dimensional bodies. *Comput. Fluids* 23:125–.

[9] Ye, T., Mittal, R., Udaykumar, H.S. and Shyy, W. 1999. An accurate Cartesian grid method for viscous incompressible flows with complex immersed boundaries. *J. Comput. Phys.* 156:209–240.

[10] Udaykumar, H.S., Mittal, R., Rampunggoon, P. and Khanna, A. 2001. A sharp interface cartesian grid method for simulating flows with complex moving boundaries. *J. Comput. Phys.* 174:345–380.

[11] Peskin C.S. 1972. Flow patterns around heart valves: a numerical method. *J. Comput. Phys.*, 10:252–271.

[12] Peskin C.S. and McQueen D.M. 1992. Cardiac Fluid Dynamics. *Critical Reviews in Biomedical Engineering*, 20:451–459.

[13] Peskin C.S. and McQueen D.M. 1997. Shared-memory parallel vector implementation of the immersed boundary method for the computation of blood flow in the beating mammalian heart. *J. of Supercomputing*, 11:213–236.

[14] Mohd-Yusof, J. 1997. Combined Immersed Boundaries/B-Splines Methods for Simulations of Flows in Complex Geometries. *CTR Annual Research Briefs*, NASA Ames/Stanford University.

[15] Fadlun, E. A., Verzicco, R., Orlandi, P., and Mohd-Yusof, J. 2000. Combined Immersed-Boundary Finite-Difference Methods for Three-Dimensional Complex Flow Simulations. *J. Comput. Physics* 161:35–60.

[16] Kim, J., Kim, D. and Choi, H. 2001. An immersed-boundary finite-volume method for simulations of flow in complex geometries. *J. Comput. Phys.* 171:132–150.

[17] Balaras, E. 2004. Modeling complex boundaries using an external force field on fixed Cartesian grids in large-eddy simulations. *Computers & Fluids*, 33:375–404.

[18] Meneveau, C., Lund, T.S., and Cabot, W. H. 1996. A Lagrangian dynamic subgrid-scale model of turbulence. *J. Fluid Mech.* **319**, 353–.

[19] Sarghini, F., Piomelli, U. and Balaras, E. 1999. Scale-similar models for large-eddy simulations. *Physics of Fluids*, 11:1596–1607.

[20] Udaykumar, H.S., Kan, H-C., Shyy, W. and Tran-Son-Tay, R. 1997. Multiphase dynamics in arbitrary geometries on fixed Cartesian grids. *J. Comput. Phys.* 137:366–405.

[21] Udaykumar H.S., Mittal R. and Shyy W. 1999. Computation od solid liquid phase fronts in the sharp interface limit on fixed grids. *J. Comput. Physics* 153:535–574.

[22] Tseng, Y.H. and Ferziger, J.H. 2003. A ghost-cell immersed boundary method for flow in complex geometry. *J. Comput. Physics*, In Press.

[23] Orlansky, I., 1976. A simple boundary condition for unbounded hyperbolic flows. *J. Comput. Phys.*, 21:251–

[24] Clift, R., Grace, J.R. and Weber, M.E. 1978. Bubbles, Drops and Particles. *Academic Press*, San Diego, CA.

[25] Johnson, T. and Patel, V. C. 1999. Flow past a sphere up to a Reynolds number of 300. *J. Fluid Mech.*, 378:10–.

[26] Hunt, J. C. R., Wray, A. A., & Moin, P. 1988. Eddies, Streams and Convergence Zones in Turbulent Flows. Center for Turbulence Research, Proceedings of the Summer Program 1988, 193.

[27] Guilmineau, E. and Queutey, P. 2002. A numerical simulation of vortex shedding from an oscillating circular cylinder. *J. of Fluid and Structures*, 16:773–794.

[28] Kiger, K. 2004. Private Communication.